Journal of Zhejiang University-SCIENCE A
www.jzus.zju.edu.cn; www.springer.com/journal/11582
E-mail: jzus_a@zju.edu.cn

Research Article
https://doi.org/10.1631/jzus.A2600200

Guided differential dilated convolutional network for fault diagnosis of hydraulic manipulators

Daocheng FU[1], Xu YANG[1]✉, Haitao LIU[2], Yugang REN[3], Xianpeng SHI[3], Limin ZHU[4]

[1]*Institute of Marine Science and Technology, Shandong University, Qingdao 266237, China*
[2]*School of Mechanical Engineering, Tianjin University, Tianjin 300354, China*
[3]*National Deep Sea Center, Qingdao 266237, China*
[4]*State Key Laboratory of Mechanical System and Vibration, Shanghai Jiao Tong University, Shanghai 200240, China*

Abstract: Fault diagnosis for hydraulic manipulators plays a crucial role in ensuring operational safety but still faces challenges in fault localization. To address this issue, a guided differential dilated convolutional network (GDDCN) is proposed in this study. First, a novel interference masking mechanism is designed to provide dual guidance for feature extraction and classification. Then, a learnable differential kernel with the center parameter fixed at zero and side parameters opposite in sign is designed to adaptively extract gradient features. Afterward, a multiscale gated dilated convolution (MGDC) module is developed to capture global temporal features across multiple scales and achieve gated feature fusion. Finally, the fused features are fed into a fully connected classification module for fault classification. The results show that the GDDCN achieves diagnosis of the faulty joint with an average accuracy of 99.39% on a hydraulic manipulator platform. The superiority and effectiveness of the GDDCN are further confirmed through comparative and ablation studies.

Key words: Hydraulic manipulator; Fault diagnosis; Dual guidance; Gradient feature; Dilated convolutional

1 Introduction

Hydraulic manipulators are widely used in deep-sea operations, industrial manufacturing, and other fields due to their advantages of fast response, strong load capacity, and broad environmental adaptability (Yang et al., 2023; Chen G et al., 2025; Liang et al., 2025). Nevertheless, the highly coupled hydraulic systems and mechanical structures of hydraulic manipulators are prone to issues such as internal leakage and valve sticking during operation. Once these faults occur, severe consequences such as abnormal system responses and operational interruption may arise, posing a serious threat to operational safety (Jose et al., 2021; Cheng et al., 2025; Meng et al., 2025). To solve this, it is necessary to localize the faulty joint for designing fault-tolerant control methods or replacing the faulty joint to restore the normal state. Therefore, it is of great significance to design a fault diagnosis method for locating the broken-down joint.

Fault diagnosis methods for manipulators can be divided into model-based and data-driven methods (Hong et al., 2025). The former construct mathematical models of the manipulator system (Wang et al., 2018, 2019) and detect faults by comparing actual operating data with outputs generated by the model. For example, Ma and Yang (2016) proposed a nonlinear adaptive observer for diagnosing actuator and sensor faults in robotic manipulators. Wu et al. (2016) developed a fault detection filter based on a Markovian jump model for underactuated manipulators. Sabry et al. (2020) built an energy consumption model to diagnose the joint faults of robotic manipulators. Such methods do not rely on large amounts of training data or extensive sensor deployment, with the advantage of relatively low diagnostic costs.

In contrast, data-driven intelligent diagnosis techniques can be applied without explicit modeling of the coupled system of manipulators by directly extracting fault features from operational data (Guan et al.,

✉ Xu YANG, xu_y@sdu.edu.cn
Xu YANG, https://orcid.org/0000-0001-9462-0507

Received Apr. 2, 2026; Revision accepted June 17, 2026;
Crosschecked Aug. 3, 2026

© Zhejiang University Press 2026

2021; Ding et al., 2025; Fan et al., 2025; Han et al., 2026). Due to the excellent performance in diagnostic accuracy and diagnosable types, data-based methods have become a research hotspot in manipulator fault diagnosis.

As a typical data-driven approach, machine learning (ML) is widely applied in fault diagnosis tasks. For example, Jose et al. (2021) employed a support vector machine (SVM) to diagnose leakage faults of hydraulic actuators. Muradore and Fiorini (2012) applied partial least squares for the fault detection of manipulators. Eski et al. (2011) implemented fault diagnosis of manipulators by means of an artificial neural network. Wu et al. (2024) used particle swarm optimization combined with random forest to achieve fault diagnosis for industrial robots. Nevertheless, traditional ML methods rely on expert knowledge to manually extract features and have limited modeling ability for nonlinear features, which restricts their learning capability, making them unsuitable for complex diagnostic tasks and diverse operational environments (Li et al., 2024).

In recent years, deep learning (DL) has demonstrated superior performance over traditional ML methods in feature extraction and fault identification for complex tasks (Wang et al., 2023; Li et al., 2025; Patil et al., 2025). In the field of manipulator fault diagnosis, Long et al. (2021) combined SVM and sparse autoencoders for industrial robot joint reducer fault diagnosis. On the basis of this work, Long et al. (2023) further proposed a DL method that incorporates a convolutional neural network (CNN) and capsule network to improve fault diagnosis performance. Jiang et al. (2025) designed a novel CNN and a loss function to diagnose the gear faults of manipulators under imbalanced samples. Wang ZX et al. (2025) fused gated recurrent units (GRUs), CNNs, and attention mechanisms for fault diagnosis of quadruped robots. Wang YM et al. (2024) developed a novel transformer model with strong generalization ability for diagnosing faults of industrial robot harmonic reducers. Bilal et al. (2024) proposed diagnosing the joint bearing faults of manipulators by using a hybrid CNN and recurrent neural network (RNN). He et al. (2024) constructed an attention residual network to diagnose compound faults in multiple joints of industrial robots, which are mainly caused by harmonic reducers. Chen et al. (2022) designed a novel CNN and a feature classification guidance function for diagnosing the faults of industrial robots. In the field of hydraulic system fault diagnosis, Yang et al. (2026) proposed a novel architecture that integrates physical information, a graph neural network (GNN), and attention mechanisms for hydraulic system fault diagnosis. Tang and Wang (2026) proposed an improved temporal CNN for hydraulic system fault diagnosis in the presence of limited samples and sensor signal absence. Wu et al. (2026) combined a generative adversarial network with contrastive learning to achieve hydraulic system fault diagnosis. DL methods have strong nonlinear modeling capabilities and can automatically extract multilayer features from data, which improves the classification accuracy and demonstrates their great potential in large-scale data-driven fault diagnosis (Miao et al., 2022).

However, existing studies mainly focus on electrically driven manipulators and general hydraulic systems (Chen C et al., 2024; Wang SJ et al., 2024; Chen SH et al., 2025; Xu et al., 2025; Yin et al., 2025). In contrast, the hydraulically driven manipulator system, which contains hydraulic power units, control valve assemblies, actuation mechanisms, and associated fluid transmission pipelines, is more complex and shows pronounced nonlinear characteristics, increasing the difficulty of fault localization (Chen G et al., 2025; Zhou et al., 2025).

To accurately localize the broken-down joint of the hydraulic manipulator, this study proposes a novel guided differential dilated convolutional network (GDDCN) that consists of a target guidance (TG) module, a learnable differential (LD) module, a multiscale gated dilated convolution (MGDC) module, and a fully connected classification (FCC) module. The key contributions are as follows:

(1) A novel TG module is constructed to guide feature extraction and classification by masking the position signals and the classification logits corresponding to untested joints, which can highlight the features of the tested joint and improve diagnostic accuracy and specificity.

(2) A channel-wise LD kernel with the center parameter fixed at zero and side parameters opposite in sign is designed to automatically learn the differential coefficients, enabling adaptive extraction of gradient features from the modified position signals.

(3) An MGDC module is developed, which combines multiscale 1D dilated convolution and a scale-gated weighted mechanism. It can effectively capture

global temporal features at different scales and achieve efficient feature fusion by scale weights, which are calculated based on the global representation of the input features.

2 Proposed GDDCN

The proposed framework of GDDCN is illustrated in Fig. 1. First, the control voltages are fed into the TG module, which masks the original position signals $\boldsymbol{X}$ from the untested joints to generate the modified position signals $\tilde{\boldsymbol{X}}$. Then, the modified position signals are sent to the LD module to extract differential features. These differential features, together with the modified position signals, are input into the MGDC module for further feature extraction. Next, the extracted features are fed into the FCC module, leading to the original classification logits. Finally, the classification result is obtained under the guidance of the TG module.

2.1 Data acquisition and preprocessing

During the data acquisition process, the position signals and control voltages of all joints are recorded simultaneously. Considering the presence of sharp

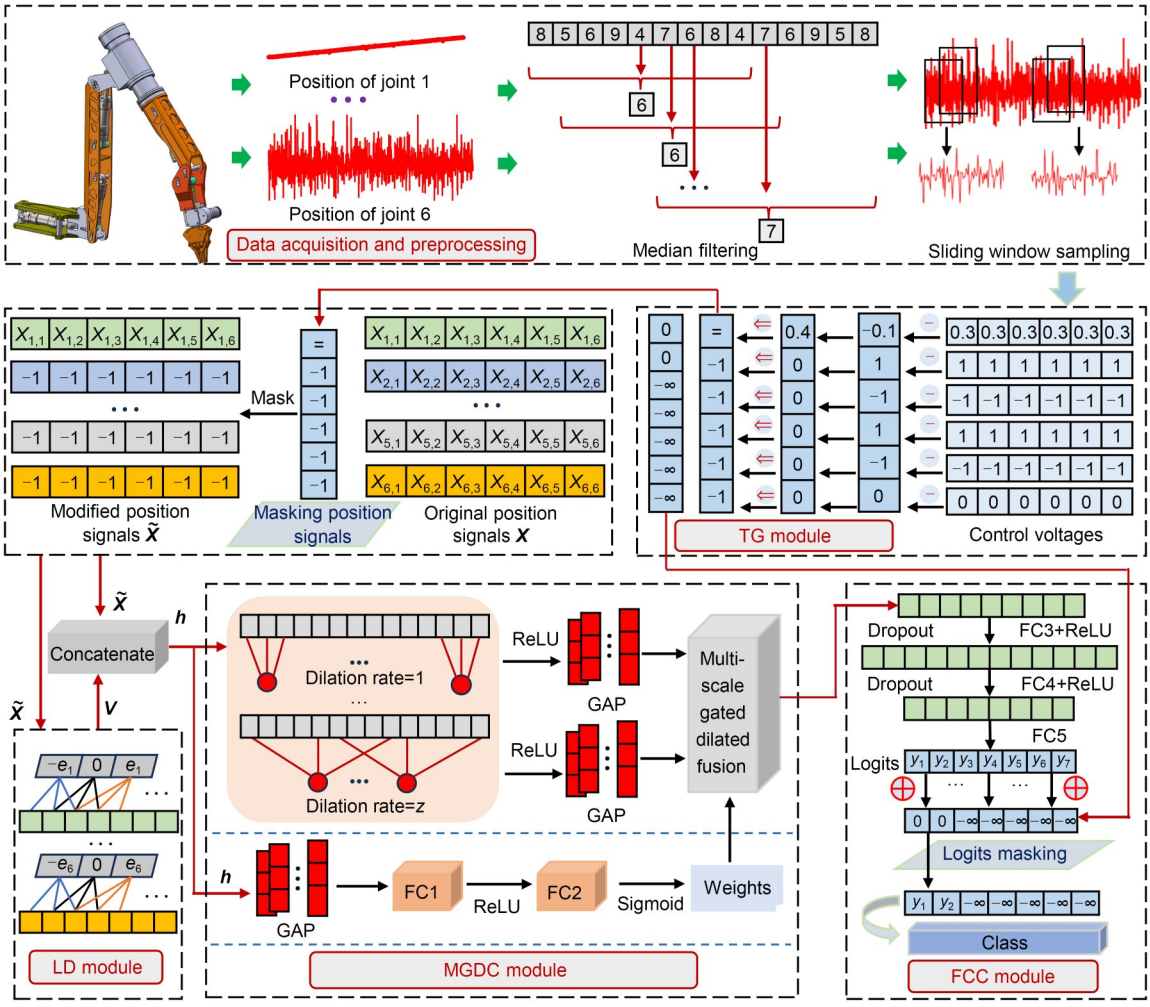


Fig. 1 Fault diagnosis framework for hydraulic manipulators based on GDDCN. $X_{c,j}$ (c=1, 2, ⋯, n; j=1, 2, ⋯, l) is the jth position signal of the cth channel in the original position signals, where n is the total number of joints, and l is the sequence length of each channel; h is the multiscale dilated convolution input sequence; V is the differential feature sequence output by the LD module; e_1–e_6 are the learnable differential parameters corresponding to the six joints; z is the total number of dilation branches; ReLU is the rectified linear unit; GAP is the global average pooling ; FC1–FC5 are the fully connected layers; y_1–y_7 are the classification logits. Note that n=6 and the first six position signals are shown in the figure as an example to illustrate the overall workflow

noise in the original position signals, this study adopts median filtering for signal preprocessing to improve signal quality (Wang SB et al., 2025).

$$x_{c,i}^{\mathrm{f}}=M\left\{x_{c,i-\frac{\rho-1}{2}},\ \cdots,\ x_{c,i},\ \cdots,\ x_{c,i+\frac{\rho-1}{2}}\right\}, \tag{1}$$

$$T=T_0-\rho+1, \tag{2}$$

where $x_{c,i}^{\mathrm{f}}$ (c=1, 2, ⋯, n; i=$\frac{\rho-1}{2}+1, \frac{\rho-1}{2}+2, \cdots, \frac{\rho-1}{2}+T$) is the ith position signal of the cth channel after the median filtering operation $M(\cdot)$, which selects the middle value within the filtering window; $x_{c,i-\frac{\rho-1}{2}}$, $x_{c,i}$, $x_{c,i+\frac{\rho-1}{2}}$ are the left-boundary, center, and right-boundary signal values within the filtering window, respectively; T is the output length after filtering; T_0 is the initial length of the joint position signal; ρ is the filtering window size, which is an odd integer.

To cover the different temporal segments of joint motion, this study adopts the sliding window sampling method after the median filtering operation. This method can generate partially overlapping subsequences by setting the sliding window length and step size, which not only increases the number of samples but also improves the robustness of the model in diagnosing different time series segments.

2.2 Target guidance module

During the data acquisition process of the hydraulic manipulator, only one joint is in motion in each experiment, and the other joints remain at their limit positions under limit position voltages. If the position signals of all joints are directly used as model inputs, the inclusion of signals from untested joints will introduce noise, which negatively affects the model's convergence speed and accuracy. To address this, this study designs a TG module that identifies the tested joint by analyzing the control voltages $\boldsymbol{U}\in\mathbb{R}^{n\times l}$, and then masks the original position signals $\boldsymbol{X}\in\mathbb{R}^{n\times l}$ to generate the modified position signals $\tilde{\boldsymbol{X}}\in\mathbb{R}^{n\times l}$. The process is as follows:

$$g_c^{\mathrm{f}}=\begin{cases}1, & \text{if } U_{c,1}\neq r_c,\\ 0, & \text{if } U_{c,1}=r_c,\end{cases} \tag{3}$$

$$\widetilde{\boldsymbol{X}}_c=\boldsymbol{X}_c\odot\boldsymbol{G}_c^{\mathrm{f}}+(\boldsymbol{\varphi}-\boldsymbol{G}_c^{\mathrm{f}})\odot\boldsymbol{\eta}, \tag{4}$$

where g_c^{f} (c=1, 2, ⋯, n) is the state binary encoding of the cth joint; $U_{c,1}$ is the first element of the cth channel of $\boldsymbol{U}$; r_c is the limit position voltage of the cth joint; $\tilde{\boldsymbol{X}}_c\in\mathbb{R}^{1\times l}$ is the cth channel of $\tilde{\boldsymbol{X}}$; $\boldsymbol{X}_c\in\mathbb{R}^{1\times l}$ is the cth channel of $\boldsymbol{X}$; $\boldsymbol{G}_c^{\mathrm{f}}\in\mathbb{R}^{1\times l}$ is the state binary encoding vector obtained by repeating g_c^{f} to match the length of $\boldsymbol{X}_c$; $\boldsymbol{\varphi}\in\mathbb{R}^{1\times l}$ is the all-ones vector; $\odot$ is the element-wise multiplication; $\boldsymbol{\eta}$ is the masking vector. This method preserves the position information of the tested joint while uniformly assigning the position values of untested joints to a masking value (outside the valid range).

To further improve the convergence speed, GDDCN guides classification by retaining the classification logits of the normal and fault classes of the tested joint while assigning negative infinity to the fault logits of the untested joints, which effectively suppresses the interference of the untested joints. The process is described as follows:

$$\lambda_c=\begin{cases}0, & \text{if } U_{c,1}\neq r_c,\\ -\infty, & \text{if } U_{c,1}=r_c,\end{cases} \tag{5}$$

$$\boldsymbol{g}_{\mathrm{class}}=[0,\ \lambda_1,\ \cdots,\ \lambda_n]^{\mathrm{T}}, \tag{6}$$

$$\tilde{\boldsymbol{y}}=\boldsymbol{y}+\boldsymbol{g}_{\mathrm{class}}, \tag{7}$$

where λ_c (c=1, 2, ⋯, n) is the classification masking value of the cth joint; $\boldsymbol{g}_{\mathrm{class}}\in\mathbb{R}^{n+1}$ adds 0 before λ_1 to preserve the classification logits of the normal class; $\boldsymbol{y}\in\mathbb{R}^{n+1}$ is the original classification logits; $\tilde{\boldsymbol{y}}\in\mathbb{R}^{n+1}$ is the modified classification logits.

2.3 Learnable differential module

Differential operations are widely used to extract gradient features from 2D images (Wei et al., 2024; Chen Y et al., 2025; Zhang et al., 2025). To extract the gradient features in the 1D position signal, this study proposes an LD module with a differential kernel $\boldsymbol{D}\in\mathbb{R}^{n\times 3}$. The differential kernel consists of a non-trainable center parameter (set to zero) and trainable parameters (equal value and opposite signs) on two sides. By performing convolution operations with this differential kernel, a differential feature sequence $\boldsymbol{V}\in\mathbb{R}^{n\times l}$ that has the same length as the input is produced. The differential operation is defined as follows:

$$\boldsymbol{D}_c=[-e_c,\ 0,\ e_c], \tag{8}$$

$$\boldsymbol{V}_c=\widetilde{\boldsymbol{X}}_c*\boldsymbol{D}_c, \tag{9}$$

where $\boldsymbol{D}_c\in\mathbb{R}^{1\times 3}$ (c=1, 2, ⋯, n) is the cth channel of $\boldsymbol{D}$; e_c is the trainable parameter; $\boldsymbol{V}_c\in\mathbb{R}^{1\times l}$ is the cth channel of $\boldsymbol{V}$; * is the convolution operation.

The LD module has the following advantages over standard fixed-difference operators and unconstrained 1D convolutions. Compared with standard fixed-difference operators, the learnable parameters in the LD module can adaptively adjust the differential intensity according to the data distribution of each channel, while the coefficients of standard fixed-difference operators are manually preset and require parameter tuning to find suitable differential coefficients. Compared with unconstrained 1D convolutions, the output of the differential kernel in the LD module has a clear physical meaning (the gradient feature of the signal). In addition, the number of parameters of the differential kernel is only one-third of the unconstrained 1D convolution with three parameters.

2.4 Multiscale gated dilated convolution module

The kernel of a standard convolution is continuous, while the kernel of dilated convolution has a certain interval. This design can expand the receptive field without increasing the number of parameters. By adjusting this interval (dilation rates), features at different time scales can be extracted (Wang et al., 2021; Liu et al., 2025). In this study, 1D multiscale dilated convolution is used to extract multiscale features from the data by setting different dilation rates. The input sequence is obtained by the following operation:

$$\boldsymbol{h}=C(\boldsymbol{V},\tilde{\boldsymbol{X}}), \tag{10}$$

where $C(\cdot)$ is the concatenate operation; $\boldsymbol{h}\in\mathbb{R}^{2n\times l}$ is the multiscale dilated convolution input sequence, obtained by concatenating $\boldsymbol{V}$ and $\tilde{\boldsymbol{X}}$ along the channel dimension. The detailed calculation of the multiscale dilated convolution operation is as follows:

$$\Gamma^{m}_{c'',k}=f\left(\sum_{c'=1}^{2n}\sum_{\tau=1}^{\varepsilon_\tau}h_{c',k+(\tau-1)d^m}w^{m}_{c'',c',\tau}+b^{m}_{c''}\right), \tag{11}$$

where $\Gamma^{m}_{c'',k}$ (k=1, 2, ⋯, ε^{m}_{1}; c''=1, 2, ⋯, $\varepsilon_{c''}$) is the kth element in the c''th channel of the output sequence of dilated convolution operation at scale m; ε^{m}_{1} is the length of k at scale m; $\varepsilon_{c''}$ is the length of c''; $f(\cdot)$ is the activation function; τ (τ=1, 2, ⋯, ε_τ) is the index within the convolution kernel; ε_τ is the length of τ; $h_{c',k+(\tau-1)d^m}$ (c'=1, 2, ⋯, $2n$) is the $(k+(\tau-1)d^m)$th element of the c'th channel of $\boldsymbol{h}$, and d^m is the dilation rate at scale m; $w^{m}_{c'',c',\tau}$ is the τth weight of the c'th channel of the c''th dilated convolution kernel at scale m; $b^{m}_{c''}$ is the c''th bias at scale m.

The multiscale dilated convolution features need to be fused. Since the receptive fields of multiscale dilated convolution are different, the lengths of the obtained feature sequences are also different. Directly fusing these multiscale outputs may lead to an imbalance among the fused features. To address this issue, this study employs a GAP method to obtain global features $\boldsymbol{p}^m$ from the output of the dilated convolution operation at scale m. The calculation formula is as follows:

$$p^{m}_{c''}=\frac{\sum_{k=1}^{\varepsilon^{m}_{1}}\Gamma^{m}_{c'',k}}{\varepsilon^{m}_{1}}, \tag{12}$$

where $p^{m}_{c''}$ is the c''th element of $\boldsymbol{p}^m$.

If the multiscale features after pooling are directly concatenated, it may lead to parameter redundancy and information dispersion. To address this, this study introduces a scale-gated fusion mechanism that adaptively assigns weights to different scale branches through a gating network. The global feature vector $\boldsymbol{\alpha}\in\mathbb{R}^{2n}$ is obtained by applying the GAP operation to $\boldsymbol{h}$. The features $\boldsymbol{p}^m$ are weighted, and then summed to produce the feature fusion vector $\boldsymbol{J}$. The scale weight calculation and multiscale dilated gated fusion process are as follows:

$$\alpha_{c'}=\frac{\sum_{k'=1}^{l}h_{c',k'}}{l}, \tag{13}$$

$$\boldsymbol{Q}=\sigma\left(L_2(R(L_1(\boldsymbol{\alpha})))\right), \tag{14}$$

$$\boldsymbol{J}=\sum_{m=1}^{z}\boldsymbol{Q}^m\odot\boldsymbol{p}^m, \tag{15}$$

where $\alpha_{c'}$ is the global average pooling result of the c'th channel of $\boldsymbol{h}$; $h_{c',k'}$ (k'=1, 2, ⋯, l) is the k'th element at the c'th channel of $\boldsymbol{h}$; $\boldsymbol{Q}\in\mathbb{R}^{z}$ is the weight vector corresponding to each scale branch; $\sigma(\cdot)$ is the sigmoid activation function; $L_1(\cdot)$ and $L_2(\cdot)$ are the FC layers; $R(\cdot)$ is the ReLU activation function; $\boldsymbol{Q}^m$ is obtained by repeating the value of $\boldsymbol{Q}$ corresponding to scale m to match the length of $\boldsymbol{p}^m$.

2.5 Fully connected classification module

By inputting the features obtained from the MGDC module into the FCC module, the original

classification logits $\boldsymbol{y}$ can be obtained. The process is as follows:

$$\boldsymbol{y}=L_5\Big(R\Big(L_4(R(L_3(\boldsymbol{J})))\Big)\Big), \tag{16}$$

where $L_3(\cdot)$, $L_4(\cdot)$, and $L_5(\cdot)$ are the FC layers. Dropout is applied after the ReLU activation function of $L_3(\cdot)$ and $L_4(\cdot)$ to prevent overfitting.

Based on the original classification logits $\boldsymbol{y}$, the modified logits $\tilde{\boldsymbol{y}}$ are generated according to Eqs. (5)–(7). The final classification result is determined by selecting the class with the maximum value from $\tilde{\boldsymbol{y}}$, while the training loss is computed using the cross-entropy loss.

2.6 General procedure of GDDCN

The signals collected from the hydraulic manipulator are processed through five steps: data acquisition and preprocessing, TG module, LD module, MGDC module, and FCC module. The details of each step are described as follows:

Step 1: after the data acquisition process, median filtering is applied to remove sharp noise from the position signals, and a sliding window is used to generate samples, including position signals and control voltages.

Step 2: a TG module is constructed based on the joint control voltages. By comparing the control voltage of each joint with its limit position voltage, the tested joint can be determined. Then, the position value of the untested joints is set to a masking value such as −1, while that of the tested joint remains unchanged.

Step 3: a channel-wise LD kernel centered at zero with opposite signs at both ends is designed to adaptively extract gradient features from the modified position signals.

Step 4: the modified position signals and their differential features are jointly input into dilated convolution branches with different dilation rates. The output of each branch is activated using the ReLU activation function, and then processed through GAP. Subsequently, a gated network adaptively allocates weights for each branch based on the global representation of the input sequence. The weighted features from all branches are summed to complete feature fusion.

Step 5: the fused features from Step 4 are input into a multilayer fully connected network to output the classification logits of each class. The guidance mechanism is reapplied to suppress the fault logits of untested joints by masking them to negative infinity while keeping the logits corresponding to the tested joint unchanged. Final classification is performed based on the modified logits.

3 Experimental verification

In this section, a hydraulic manipulator platform is constructed, and data from both normal and faulty operating conditions are collected. Subsequently, the superiority and effectiveness of the GDDCN are validated through comparative and ablation studies.

3.1 Platform setup and data acquisition

To verify the effectiveness of the GDDCN, a hydraulic manipulator platform of six degrees of freedom is constructed, as shown in Fig. 2. The hydraulic manipulator consists of six active joints, where joints 1, 2, 3, and 5 are driven by the hydraulic cylinder equipped with a displacement sensor, joint 4 is driven by a hydraulic rotary actuator equipped with a resolver, and joint 6 is driven by a hydraulic motor equipped with an angle sensor. The position state of the manipulator can be monitored in real time.

Faults in the hydraulic manipulator may originate from the electrical control system, hydraulic system, or mechanical structure. It is very difficult to directly pinpoint the source of the fault. Nevertheless, regardless of the source, it will ultimately affect the motion performance of the joint.

Based on the flow equation of the proportional valve, the flow continuity equation of the actuator, and the force balance equation of the actuator (Feng et al., 2021), the motion of the hydraulic actuator can be described by the following transfer function:

$$X_{\mathrm{lap}}=\frac{K_U\dfrac{K_2}{A_\mathrm{p}}U_{\mathrm{lap}}-K_F\dfrac{K_4}{A_\mathrm{p}^2}\left(1+\dfrac{O_\mathrm{t}}{4\beta K_4}s\right)F_{\mathrm{lap}}}{s\left(\dfrac{s^2}{\omega^2}+\dfrac{2\zeta}{\omega}s+1\right)}, \tag{17}$$

where X_{lap} is the displacement (linear or angular) response of the hydraulic actuator; K_U is the voltage fault coefficient; K_2 is the flow gain coefficient; A_p is the effective piston area of the hydraulic cylinder or

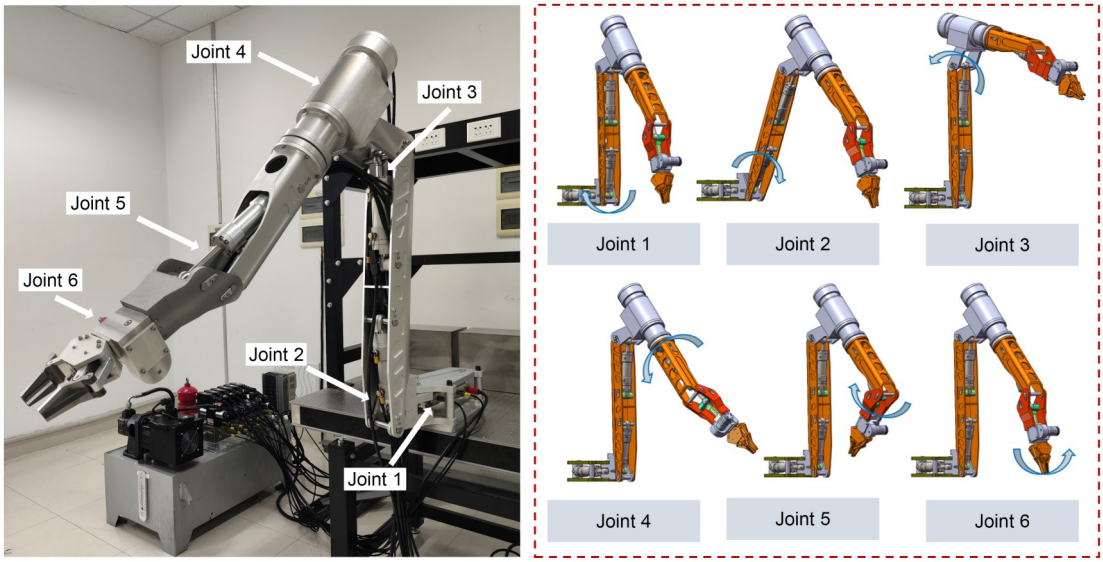


Fig. 2 (a) Hydraulic manipulator experimental platform; (b) schematic diagram of joint motion

displacement of the hydraulic motor; U_{lap} is the control voltage command; K_F is the load fault coefficient; K_4 is the total flow pressure coefficient; β is the effective bulk modulus; O_t is the total compression volume; s is the Laplace variable; F_{lap} is the external load value (force or torque); ω is the natural frequency; ζ is the damping ratio.

Two types of faults (gain fault and failure fault) are defined based on the transfer function. It is regarded as a gain fault if $K_U \neq 1$, indicating that the displacement response is abnormal under the same control voltage input. Additionally, it is regarded as a failure fault if $K_U=0$ and $K_F=0$, indicating that the joint does not respond at all regardless of the input U_{lap} and load F_{lap}.

The experimental procedure for data acquisition is as follows. First, limit position voltages are applied to all joints to drive them to their respective mechanical limits. Then, each of the six joints is sequentially selected as the tested target. To collect data under normal operating conditions, the tested joint performs reciprocating motion under a normal voltage while the other joints remain at their limit positions. Next, a gain fault is simulated by changing the control voltage of the tested joint from a normal voltage to a gain voltage ($K_U \neq 1$), while all other joints remain fixed at their limit positions. Thus, the dynamic response of the tested joint differs from that under normal conditions. Furthermore, a failure fault ($K_U=0$ and $K_F=0$) is simulated by cutting off the power supply to the proportional valve of the tested joint, resulting in no motion response under the normal voltage, while all other joints remain at their limit positions. Table 1 lists the limit position voltage, normal voltage, and gain voltage for each joint.

Following the collection of signals at a sampling frequency of 200 Hz, the position signals are processed by applying median filtering with a window size of 9 and a step size of 1. Then, the position signals and control voltages are sampled using the sliding window method, with a window size of 100 (corresponding to 0.5 s) and a step size of 10. The size of the samples is shown in Table 2. Each sample consists of 12 channels, and each channel contains 100 elements. For each sample, channels 1–6 correspond to the position signals of six joints, respectively, while channels 7–12 correspond to the control voltages of six joints, respectively. The number of samples differs for each joint state.

Table 1 Limit position voltage, normal voltage, and gain voltage of each joint of the manipulator

Joint	Limit position voltage (V)	Normal voltage (V)	Gain voltage (V)
1	−0.10	0.30	0.26
2	1.00	−0.16	−0.12
3	−1.00	0.30	0.26
4	1.00	−0.30	−0.26
5	−1.00	0.44	0.40
6	0.00	1.00	0.70

Table 2 Sample size for training and testing

Joint state	Sample size		Class
	Training dataset	Test dataset	
Normal-joint 1	297×12×100	148×12×100	1
Normal-joint 2	112×12×100	57×12×100	1
Normal-joint 3	292×12×100	146×12×100	1
Normal-joint 4	154×12×100	79×12×100	1
Normal-joint 5	376×12×100	186×12×100	1
Normal-joint 6	266×12×100	132×12×100	1
Gain fault-joint 1	366×12×100	182×12×100	2
Failure fault-joint 1	190×12×100	90×12×100	2
Gain fault-joint 2	164×12×100	84×12×100	3
Failure fault-joint 2	190×12×100	90×12×100	3
Gain fault-joint 3	393×12×100	194×12×100	4
Failure fault-joint 3	190×12×100	90×12×100	4
Gain fault-joint 4	215×12×100	109×12×100	5
Failure fault-joint 4	190×12×100	90×12×100	5
Gain fault-joint 5	431×12×100	216×12×100	6
Failure fault-joint 5	190×12×100	90×12×100	6
Gain fault-joint 6	403×12×100	199×12×100	7
Failure fault-joint 6	190×12×100	90×12×100	7

3.2 Evaluation metrics and model parameters

In this study, four performance evaluation metrics (accuracy, precision, recall, and F1-score) are employed. Considering the imbalance of samples among different classes, macroaverage precision (MP), macroaverage recall (MR), and macroaverage F1-score (MF1) are adopted (Liu et al., 2024). The formulas of the four metrics are as follows:

$$A_{\mathrm{acc}}=\frac{\sum_{\delta=1}^{\mu} n_{\mathrm{TP},\delta}}{N}, \tag{18}$$

$$P_{\mathrm{M}}=\frac{1}{\mu}\sum_{\delta=1}^{\mu}\frac{n_{\mathrm{TP},\delta}}{n_{\mathrm{TP},\delta}+n_{\mathrm{FP},\delta}}, \tag{19}$$

$$R_{\mathrm{M}}=\frac{1}{\mu}\sum_{\delta=1}^{\mu}\frac{n_{\mathrm{TP},\delta}}{n_{\mathrm{TP},\delta}+n_{\mathrm{FN},\delta}}, \tag{20}$$

$$F_{\mathrm{1,M}}=\frac{2P_{\mathrm{M}}R_{\mathrm{M}}}{P_{\mathrm{M}}+R_{\mathrm{M}}}, \tag{21}$$

where A_{acc} is the accuracy; N is the total number of samples in the test dataset; μ is the total number of classes; $n_{\mathrm{TP},\delta}$ is the number of samples correctly predicted as class δ (true positives for class δ); P_{M} is the macroaverage precision; $n_{\mathrm{FP},\delta}$ is the number of samples incorrectly predicted as class δ (false positives for class δ); R_{M} is the macroaverage recall; $n_{\mathrm{FN},\delta}$ is the number of samples belonging to class δ but incorrectly predicted as another class (false negatives for class δ); $F_{\mathrm{1,M}}$ is the macroaverage F1-score.

The experiments are conducted using PyTorch 2.3.0 with CUDA 11.8 on an Intel Core i7-10870H CPU and an NVIDIA GeForce RTX 2060 GPU. The model is trained for 200 epochs using the Adam optimizer with an initial learning rate of 0.0001 and batch size of 64. A learning rate decay strategy is employed with a step size of 80 epochs and a decay factor of 0.5. The specific parameter settings of the MGDC module and the subsequent FCC module are shown in Fig. 3. 'In' and 'out' represent the input channel and

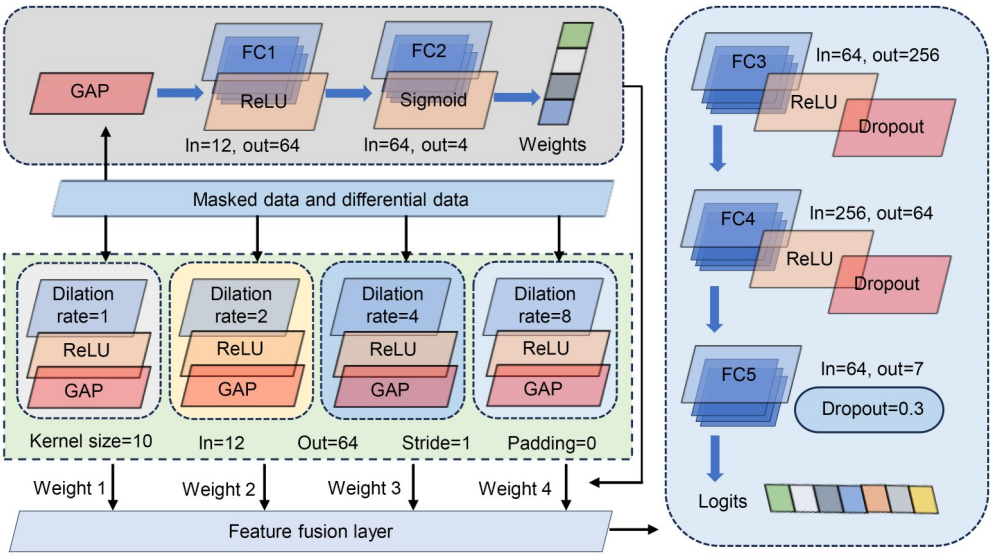


Fig. 3 Parameter settings of the MGDC module and the FCC module

output channel, respectively. The settings of kernel size, input channel, output channel, stride, and padding are consistent across the different dilated branches.

3.3 Comparative study

3.3.1 Impact of position signal and logit masking in the TG module

The TG module integrates position signal masking and classification logits masking to provide guidance for feature extraction and classification. To validate its effectiveness, this section compares GDDCN with three variants, including a method without any masking operation (G0DDCN), a method that only masks position signals (G1DDCN), and a method that only masks classification logits (G2DDCN). The accuracy comparison curves are shown in Fig. 4. Each point is the average accuracy of 10 consecutive epochs. G2DDCN shows slightly higher accuracy than GDDCN during the early stages but demonstrates poorer convergence performance, which reflects the limitations of guidance solely at the classification. Although G1DDCN eventually achieves an accuracy close to that of GDDCN, its accuracy during early epochs is noticeably lower than that of GDDCN. The comparison results indicate that the guidance of feature extraction and classification are complementary, confirming the effectiveness of the dual guidance mechanism in enhancing model performance.

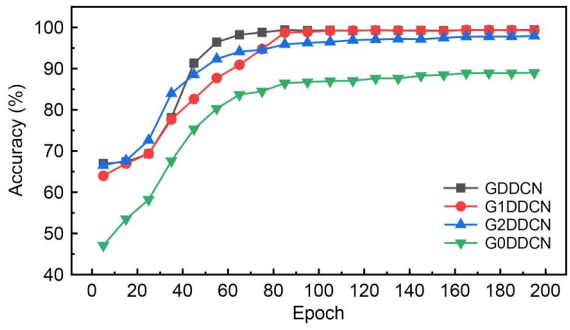


Fig. 4 Comparison of different approaches using TG module

To investigate the influence of different position masking values η, four masking values (-1, -3, -5, and -10) are tested. The accuracy comparison curves are shown in Fig. 5. When the position masking value is -1, the accuracy increases rapidly and achieves the best convergence. As the masking value gradually decreases to -3, -5, and -10, the accuracy improvement

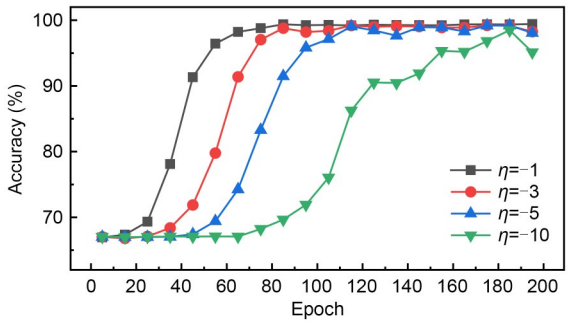


Fig. 5 Comparison under different position masking values

becomes gradually slower, and it shows oscillations in later epochs. This indicates that the position masking value should be set within an appropriate range to be effectively processed by the model.

3.3.2 Comparison between using the LD module and using fixed-parameter differential methods

To validate the superiority of the LD kernel, experiments are designed to compare it with fixed-parameter differential kernels set to values of 1, 10, and 20. The fixed kernel parameters are kept constant and not updated during training. The experimental results are shown in Fig. 6. When the fixed kernel parameters are set to 1, 10, and 20, corresponding to GD-1-DCN, GD-10-DCN, and GD-20-DCN, respectively, there are significant differences in the model's accuracy. In contrast, the proposed GDDCN can automatically learn the appropriate kernel parameters and achieve superior performance simultaneously.

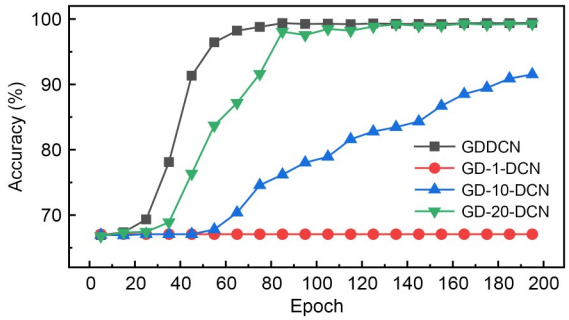


Fig. 6 Comparison under different kernel parameters

To clearly study the training process of the differential kernel parameters across the six channels, Fig. 7 presents their variation curves with respect to training epochs. The kernel parameters continuously adjust from their initial values (the parameters are initialized uniformly in the range of $[-1, 1]$), and eventually converge

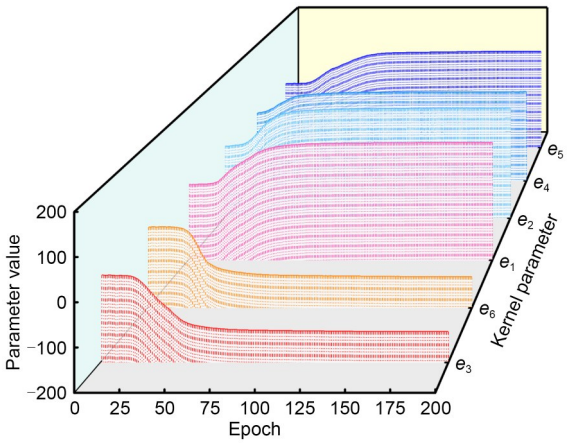


Fig. 7 Changes in differential kernel parameters across epochs

to the parameters suitable for the model, which improves the adaptability of gradient feature extraction.

3.3.3 Comparison using a single-scale dilated convolution branch in the MGDC module

After the LD module, this study further introduces an MGDC module based on four dilation rates of 1, 2, 4, and 8 to enhance the feature extraction capability. To investigate the impact of multiscale settings on diagnostic performance, comparative experiments are designed by constructing four models, each retaining a single dilation rate branch (named GDDCN-1, GDDCN-2, GDDCN-4, and GDDCN-8). Their performance is compared with GDDCN. To mitigate randomness, the final performance metrics are reported as the average of the last 20 epochs (denoted as average accuracy, MP, MR, and MF1).

As shown in Table 3, the evaluation metrics of GDDCN-1 (traditional convolution) and GDDCN-8 are below 99.00%, while GDDCN-2 and GDDCN-4 show better performance, which suggests that moderate dilation rates have advantages in feature extraction. In contrast, the proposed GDDCN achieves an average accuracy of 99.39% and outperforms other models in overall performance, validating the effectiveness of the multiscale convolution structure in enhancing feature extraction capability.

Table 3 Comparison between GDDCN and single dilation rate models

Model	Average accuracy (%)	MP (%)	MR (%)	MF1 (%)
GDDCN	99.39	99.53	99.50	99.51
GDDCN-1	98.62	98.85	98.99	98.92
GDDCN-2	99.03	99.15	99.30	99.22
GDDCN-4	99.04	99.18	99.29	99.23
GDDCN-8	98.39	98.58	98.89	98.73

3.3.4 Comparison with using global max pooling in the MGDC module

To produce uniform-length sequences of global features, a global pooling operation is introduced after multiscale feature extraction. To investigate the impact of pooling methods on model performance, a comparative experiment between GAP and global max pooling (GMP) is conducted. The experimental result in Fig. 8 indicates that GAP outperforms GMP across four evaluation metrics, and therefore is more suitable for the feature compression strategy.

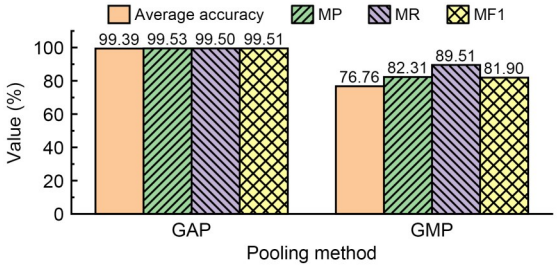


Fig. 8 Comparison between GAP and GMP

3.3.5 Comparison with prevalent DL methods

To further validate the superiority of the proposed GDDCN, comparative experiments are carried out with several DL models, including the CNN, RNN, GRU, long short-term memory (LSTM), multi-head attention (MHA), CNN-GRU, CNN-LSTM, and CNN-MHA. Fig. 9 shows the accuracy, MP, MR, and MF1 for each method under different training epochs (20 and 200). The accuracy and MF1 of most DL models converge to values below 70.00%, their MR converges to values below 90.00%, and their MP converges to values below 60.00%. Moreover, the evaluation metrics of most models show little improvement from epoch 20 to 200, indicating that their learning capacity is limited. Among them, CNN-MHA performs relatively good, with accuracy exceeding 75.00%, MP and MF1 exceeding 80.00%, and MR exceeding 90.00%. In contrast, the metrics of the proposed GDDCN converge to values approaching 100.00% and show significant improvements from epoch 20 to 200. These results further validate the superiority of GDDCN.

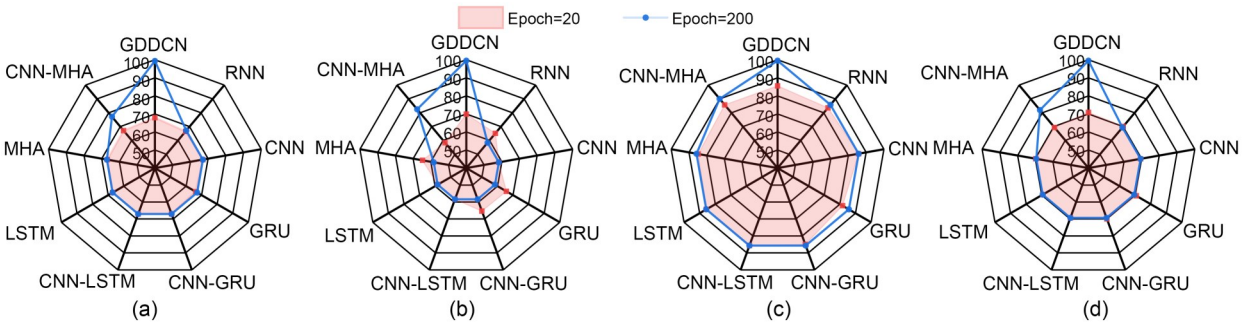


Fig. 9 Comparison with widely used DL models at different epochs (unit: %): (a) accuracy; (b) MP; (c) MR; (d) MF1

3.4 Ablation study

To further evaluate the effectiveness of the GDDCN, ablation studies are conducted. The ablation models include GDDCN without the TG module (DDCN), GDDCN without the LD module (GDCN), and GDDCN without the MGDC module (GDN). Table 4 presents the comparison results of GDDCN with ablation models across four evaluation metrics. The average accuracy, MP, MR, and MF1 of DDCN and GDCN are all lower than 90.00%, while GDN is close to 98.00%. In contrast, the corresponding metrics of GDDCN are 99.39%, 99.53%, 99.50%, and 99.51%, respectively, which outperform the ablation models and demonstrate its effectiveness in overall performance.

Table 4 Performance comparison of the GDDCN and its variants

Model	Average accuracy (%)	MP (%)	MR (%)	MF1 (%)
GDDCN	99.39	99.53	99.50	99.51
DDCN	88.96	87.64	87.47	87.48
GDCN	67.08	58.37	85.71	69.38
GDN	97.65	97.91	98.49	98.17

To visually demonstrate the advantages of GDDCN over GDCN and DDCN, Fig. 10 presents the confusion matrices of the three methods. The GDCN has difficulty distinguishing normal and broken-down joints because of the lack of differential features; the DDCN is prone to confusing faults in different joints due to the lack of a TG module. These results further confirm the importance of incorporating differential feature extraction and TG mechanisms for accurate fault identification.

To show the superiority of GDDCN over GDN, Fig. 11 shows the classification results of these two methods for each class in the test dataset. In Fig. 11, the regions divided by the joint state boundary in class 1 correspond to the normal samples of joints 1 to 6, and the regions in classes 2 to 7 represent the gain and failure faults of each joint, respectively (details can be found in Table 5). It can be observed that GDDCN and GDN perform well in identifying failure faults. However, the majority of the samples that are misclassified by GDDCN are also incorrectly labeled by GDN, and GDN exhibits more misclassifications in the identification of gain failures. This indicates that GDDCN is more effective in distinguishing gain faults.

4 Conclusions

To address the challenges of fault localization, a GDDCN is proposed in this study. First, a TG module is designed to jointly guide feature extraction and classification decisions, making the model more attentive to the features of the tested joint. Then, an LD kernel with its center parameter fixed at zero and side parameters opposite in sign is introduced to adaptively capture gradient features from positional signals. Finally, a multiscale dilated convolution combined with a scale fusion strategy effectively extracts cross-scale global features. The effectiveness of these modules is validated on a hydraulic manipulator platform. The main conclusions are as follows:

(1) The proposed GDDCN achieves an average classification accuracy of 99.39% in the test dataset of the hydraulic manipulator platform. It outperforms the ablation variants and widely used methods in four evaluation metrics, which indicates its advantage in overall performance.

(2) The comparative study shows that the guidance of feature extraction and classification has

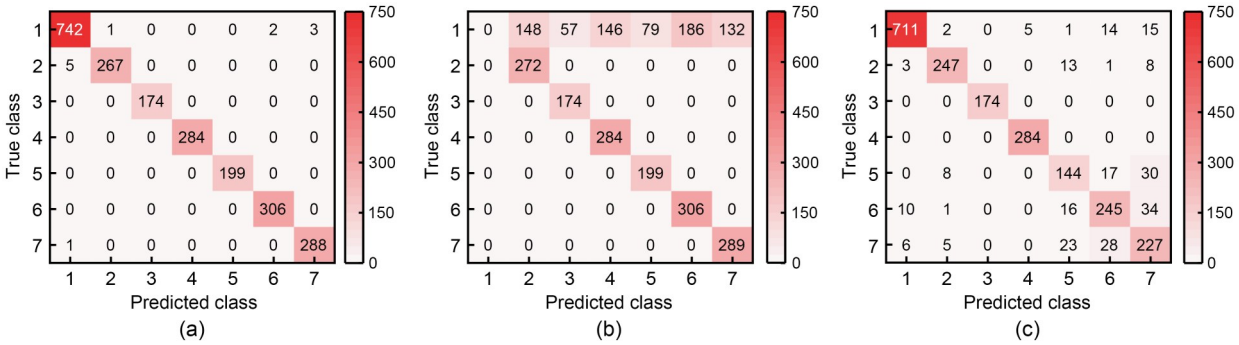


Fig. 10 Confusion matrices using (a) GDDCN, (b) GDCN, and (c) DDCN

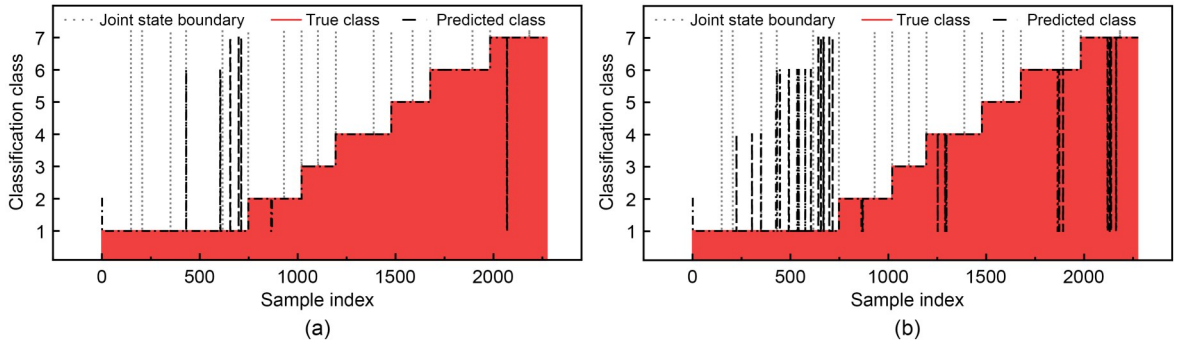


Fig. 11 Classification results during the test dataset using (a) GDDCN and (b) GDN

Table 5 Regional interpretations of samples per category

Joint state	Classification class	Region
Normal-joint 1	1	1
Normal-joint 2	1	2
Normal-joint 3	1	3
Normal-joint 4	1	4
Normal-joint 5	1	5
Normal-joint 6	1	6
Gain fault-joint 1	2	1
Failure fault-joint 1	2	2
Gain fault-joint 2	3	1
Failure fault-joint 2	3	2
Gain fault-joint 3	4	1
Failure fault-joint 3	4	2
Gain fault-joint 4	5	1
Failure fault-joint 4	5	2
Gain fault-joint 5	6	1
Failure fault-joint 5	6	2
Gain fault-joint 6	7	1
Failure fault-joint 6	7	2

complementary effects. The LD kernel can update its parameters automatically, demonstrating stronger adaptability than the traditional fixed-parameter difference operator. The performance of the MGDC module is superior to that of its single-scale version, and GAP is more effective than GMP in extracting features. Comparative experiments with several mainstream DL methods demonstrate that GDDCN exhibits significant advantages in diagnosis.

(3) The ablation study shows that the absence of the TG module leads to confusion among joint faults, the lack of the LD module impairs the model's ability to distinguish normal from faulty states, and removing the MGDC module diminishes the ability to identify gain faults despite achieving an average accuracy of 97.65%. These results validate the effectiveness of GDDCN.

Although GDDCN has achieved strong results in both comparative and ablation studies, the following limitations and challenges still exist. First, the current diagnosis can only locate the faulty joint but cannot further identify the faulty components within the joint. Second, this experiment was completed in a conventional environment, and the effectiveness of the model in harsh environments such as underwater environments needs to be further verified. In the future, we will conduct relevant research in response to the above limitations. Meanwhile, fault-tolerant control strategies will

be developed based on the diagnostic results to ensure the performance of the joints in case of faults.

Acknowledgments

This work is supported by the National Natural Science Foundation of China (No. 52175018) and the Taishan Scholars Program (Nos. tsqn202507038 and tsqn202408291), China.

Author contributions

Daocheng FU: conceptualization, data curation, formal analysis, investigation, methodology, validation, visualization, and writing–original draft, review & editing. Xu YANG: conceptualization, data curation, formal analysis, funding acquisition, methodology, project administration, resources, validation, and writing–review & editing. Haitao LIU: investigation. Yugang REN: funding acquisition. Xianpeng SHI: resources. Limin ZHU: supervision.

Conflict of interest

Daocheng FU, Xu YANG, Haitao LIU, Yugang REN, Xianpeng SHI, and Limin ZHU declare that they have no conflicts of interest.

Declaration on the use of generative AI tools

No generative AI tools were used in the preparation of this manuscript.

Data availability

The data that support the findings of this study are available from the corresponding author upon reasonable request.

References

Bilal H, Obaidat MS, Aslam MS, et al., 2024. Online fault diagnosis of industrial robot using IoRT and hybrid deep learning techniques: an experimental approach. *IEEE Internet of Things Journal*, 11(19):31422-31437. https://doi.org/10.1109/JIOT.2024.3418352

Chen C, Wang T, Lu KJ, et al., 2024. Compact convolutional transformers-generative adversarial network for compound fault diagnosis of industrial robot. *Engineering Applications of Artificial Intelligence*, 138:109315. https://doi.org/10.1016/j.engappai.2024.109315

Chen G, Wu W, Yang CG, et al., 2025. Practical finite-time observer-based adaptive backstepping super-twisting sliding mode control for deep-sea hydraulic manipulator. *IEEE Transactions on Industrial Electronics*, 72(9):9569-9579. https://doi.org/10.1109/TIE.2025.3541284

Chen LR, Cao JF, Wu K, et al., 2022. Application of generalized frequency response functions and improved convolutional neural network to fault diagnosis of heavy-duty industrial robot. *Robotics and Computer-Integrated Manufacturing*, 73:102228. https://doi.org/10.1016/j.rcim.2021.102228

Chen SH, Zheng XJ, Wu HY, 2025. A multi-rate sensor fusion and multi-task learning network for concurrent fault diagnosis of hydraulic systems. *Digital Signal Processing*, 156:104796. https://doi.org/10.1016/j.dsp.2024.104796

Chen Y, Chen SM, Liu HL, et al., 2025. Low-light image enhancement network based on central difference convolution. *Engineering Applications of Artificial Intelligence*, 158:111492. https://doi.org/10.1016/j.engappai.2025.111492

Cheng M, Li RM, Ding RQ, et al., 2025. Online terminal force estimation of hydraulic manipulator with prior torque variance. *IEEE Transactions on Instrumentation and Measurement*, 74:7502611. https://doi.org/10.1109/TIM.2025.3546374

Ding SY, Liang DG, Li ZY, et al., 2025. Data-driven design of distributed Kalman filter-based fault diagnosis for large-scale systems. *IEEE Transactions on Industrial Informatics*, 21(7):5308-5318. https://doi.org/10.1109/TII.2025.3552715

Eski I, Erkaya S, Savas S, et al., 2011. Fault detection on robot manipulators using artificial neural networks. *Robotics and Computer-Integrated Manufacturing*, 27(1):115-123. https://doi.org/10.1016/j.rcim.2010.06.017

Fan CZ, Zhang YC, Ma H, et al., 2025. A novel lightweight DDPM-based data augmentation method for rotating machinery fault diagnosis with small sample. *Mechanical Systems and Signal Processing*, 232:112741. https://doi.org/10.1016/j.ymssp.2025.112741

Feng H, Ma W, Yin CB, et al., 2021. Trajectory control of electro-hydraulic position servo system using improved PSO-PID controller. *Automation in Construction*, 127:103722. https://doi.org/10.1016/j.autcon.2021.103722

Guan Y, Meng Z, Sun DY, et al., 2021. 2MNet: multi-sensor and multi-scale model toward accurate fault diagnosis of rolling bearing. *Reliability Engineering & System Safety*, 216:108017. https://doi.org/10.1016/j.ress.2021.108017

Han JH, Wang LP, Wang D, et al., 2026. Understanding thermodynamic mechanisms of 6-DOF thermal errors in complex manufacturing feed systems via a novel interpretable network with learned activation functions. *International Journal of Machine Tools and Manufacture*, 218:104390. https://doi.org/10.1016/j.ijmachtools.2026.104390

He YM, Zhao C, Zhou X, et al., 2024. MJAR: a novel joint generalization-based diagnosis method for industrial robots with compound faults. *Robotics and Computer-Integrated Manufacturing*, 86:102668. https://doi.org/10.1016/j.rcim.2023.102668

Hong RD, Nie SL, Ji H, et al., 2025. Physics-informed machine learning for high-speed on/off valve performance degradation prediction in water hydraulic manipulator. *Reliability Engineering & System Safety*, 261:111106. https://doi.org/10.1016/j.ress.2025.111106

Jiang YL, Zhou X, Wang MY, et al., 2025. Global convolutional network and sample weighted loss for the robust

gear fault diagnosis of reciprocating manipulator. *IEEE Transactions on Instrumentation and Measurement*, 74: 3506610.
https://doi.org/10.1109/TIM.2025.3529568

Jose JT, Das J, Mishra SK, et al., 2021. Early detection and classification of internal leakage in boom actuator of mobile hydraulic machines using SVM. *Engineering Applications of Artificial Intelligence*, 106:104492.
https://doi.org/10.1016/j.engappai.2021.104492

Li CY, Hu YH, Jiang JW, et al., 2024. Fault diagnosis of a marine power-generation diesel engine based on the Gramian angular field and a convolutional neural network. *Journal of Zhejiang University-SCIENCE A*, 25(6):470-482.
https://doi.org/10.1631/jzus.A2300273

Li RR, Xia TB, Jiang YM, et al., 2025. Deep complex wavelet denoising network for interpretable fault diagnosis of industrial robots with noise interference and imbalanced data. *IEEE Transactions on Instrumentation and Measurement*, 74:3508411.
https://doi.org/10.1109/TIM.2025.3540131

Liang XL, Yao ZK, Deng WX, et al., 2025. Adaptive neural network finite-time tracking control for uncertain hydraulic manipulators. *IEEE/ASME Transactions on Mechatronics*, 30(1):645-656.
https://doi.org/10.1109/TMECH.2024.3396493

Liu XY, Wang YC, Chen TE, et al., 2024. Monitoring water quality parameters of freshwater aquaculture ponds using UAV-based multispectral images. *Ecological Indicators*, 167:112644.
https://doi.org/10.1016/j.ecolind.2024.112644

Liu Y, Jiang ZP, Zhang N, et al., 2025. Resformer: an end-to-end framework for fault diagnosis of governor valve actuator in the coupled scenario of data scarcity and high noise. *Mechanical Systems and Signal Processing*, 224:112125.
https://doi.org/10.1016/j.ymssp.2024.112125

Long JY, Mou JD, Zhang LW, et al., 2021. Attitude data-based deep hybrid learning architecture for intelligent fault diagnosis of multi-joint industrial robots. *Journal of Manufacturing Systems*, 61:736-745.
https://doi.org/10.1016/j.jmsy.2020.08.010

Long JY, Qin YX, Yang Z, et al., 2023. Discriminative feature learning using a multiscale convolutional capsule network from attitude data for fault diagnosis of industrial robots. *Mechanical Systems and Signal Processing*, 182:109569.
https://doi.org/10.1016/j.ymssp.2022.109569

Ma HJ, Yang GH, 2016. Simultaneous fault diagnosis for robot manipulators with actuator and sensor faults. *Information Sciences*, 366:12-30.
https://doi.org/10.1016/j.ins.2016.05.016

Meng LK, Wu DF, Gao H, et al., 2025. Multi-objective optimization of a wet electromagnet-driven water hydraulic high-speed on/off valve for underwater manipulator in deep sea. *Measurement*, 239:115443.
https://doi.org/10.1016/j.measurement.2024.115443

Miao ZM, Zhou FY, Yuan XF, et al., 2022. Multi-heterogeneous sensor data fusion method via convolutional neural network for fault diagnosis of wheeled mobile robot. *Applied Soft Computing*, 129:109554.
https://doi.org/10.1016/j.asoc.2022.109554

Muradore R, Fiorini P, 2012. A PLS-based statistical approach for fault detection and isolation of robotic manipulators. *IEEE Transactions on Industrial Electronics*, 59(8):3167-3175.
https://doi.org/10.1109/TIE.2011.2167110

Patil SS, Salunkhe VG, Jadhav PS, et al., 2025. A novel bearing faults diagnosis of rotor-bearing systems based on vibration responses and convolutional neural network. *Mechanical Systems and Signal Processing*, 236:113055.
https://doi.org/10.1016/j.ymssp.2025.113055

Sabry AH, Nordin FH, Sabry AH, et al., 2020. Fault detection and diagnosis of industrial robot based on power consumption modeling. *IEEE Transactions on Industrial Electronics*, 67(9):7929-7940.
https://doi.org/10.1109/TIE.2019.2931511

Tang ZH, Wang JC, 2026. Frequency-informed feature fusion framework with mask-based data augmentation for fault diagnosis of hydraulic systems under limited and missing multi-sensor data. *Flow Measurement and Instrumentation*, 110:103373.
https://doi.org/10.1016/j.flowmeasinst.2026.103373

Wang D, Wu J, Wang LP, et al., 2018. A postprocessing strategy of a 3-DOF parallel tool head based on velocity control and coarse interpolation. *IEEE Transactions on Industrial Electronics*, 65(8):6333-6342.
https://doi.org/10.1109/TIE.2017.2784378

Wang D, Wang LP, Wu J, et al., 2019. An experimental study on the dynamics calibration of a 3-DOF parallel tool head. *IEEE/ASME Transactions on Mechatronics*, 24(6):2931-2941.
https://doi.org/10.1109/TMECH.2019.2942622

Wang D, Han C, Wang LP, et al., 2023. Surface roughness prediction of large shaft grinding via attentional CNN-LSTM fusing multiple process signals. *The International Journal of Advanced Manufacturing Technology*, 126(11-12): 4925-4936.
https://doi.org/10.1007/s00170-023-11454-6

Wang F, Liu RN, Hu QH, et al., 2021. Cascade convolutional neural network with progressive optimization for motor fault diagnosis under nonstationary conditions. *IEEE Transactions on Industrial Informatics*, 17(4):2511-2521.
https://doi.org/10.1109/TII.2020.3003353

Wang SB, Chen BY, Cheng Y, et al., 2025. Investigation on morphological filtering via enhanced adaptive time-varying structural element for bearing fault diagnosis. *Measurement*, 244:116466.
https://doi.org/10.1016/j.measurement.2024.116466

Wang SJ, Tao JF, Jiang QC, et al., 2024. Manipulator joint fault localization for intelligent flexible manufacturing based on reinforcement learning and robot dynamics. *Robotics and Computer-Integrated Manufacturing*, 86:102684.
https://doi.org/10.1016/j.rcim.2023.102684

Wang YM, He YM, Kang B, et al., 2024. ProbSparse attention-based fault diagnosis for industrial robots under different working conditions. *IEEE Transactions on Instrumentation and Measurement*, 73:3514512.
https://doi.org/10.1109/TIM.2024.3374323

Wang ZX, Li HP, Chen ZY, et al., 2025. A fault diagnosis method for quadruped robot based on hybrid deep neural networks. *IEEE Transactions on Industrial Informatics*, 21(4):3027-3036. https://doi.org/10.1109/TII.2024.3523534

Wei KK, Luo WQ, Huang JW, 2024. Color image steganalysis based on pixel difference convolution and enhanced transformer with selective pooling. *IEEE Transactions on Information Forensics and Security*, 19:9970-9983. https://doi.org/10.1109/TIFS.2024.3486027

Wu JH, Yang Y, Tang XH, et al., 2026. High-accuracy few-shot fault diagnosis for smart hydraulic systems using contrastive learning enhanced categorical generative adversarial network. *Engineering Applications of Artificial Intelligence*, 176(Pt 1):114593. https://doi.org/10.1016/j.engappai.2026.114593

Wu LG, Luo WS, Zeng Y, et al., 2016. Fault detection for underactuated manipulators modeled by Markovian jump systems. *IEEE Transactions on Industrial Electronics*, 63(7): 4387-4399. https://doi.org/10.1109/TIE.2016.2541087

Wu YF, Bai Y, Yang S, et al., 2024. Extracting random forest features with improved adaptive particle swarm optimization for industrial robot fault diagnosis. *Measurement*, 229:114451. https://doi.org/10.1016/j.measurement.2024.114451

Xu WN, Zhang JG, Li HQ, 2025. Compound fault diagnosis of hydraulic system based on sample screening and joint analysis with pressure sensors pairs. *Advanced Engineering Informatics*, 68:103621. https://doi.org/10.1016/j.aei.2025.103621

Yang BS, Huang YF, Sun G, 2026. A physics-informed graph attention network with sparse temporal block selection for aircraft hydraulic system fault diagnosis. *Aerospace Science and Technology*, 175:112040. https://doi.org/10.1016/j.ast.2026.112040

Yang X, Liu X, Li SZ, et al., 2023. Core-drilling kinematic modeling and analysis of Jiaolong submersible manipulator. *Journal of Zhejiang University-SCIENCE A*, 24(11): 937-948. https://doi.org/10.1631/jzus.A2200484

Yin XC, Guo Y, Fan JW, et al., 2025. Cycloidal gear faults' detection of industrial robot joint based on IAS signal under operating. *IEEE Transactions on Instrumentation and Measurement*, 74:9505309. https://doi.org/10.1109/TIM.2025.3544734

Zhang JM, Zhang SG, Li DW, et al., 2025. Crack segmentation network via difference convolution-based encoder and hybrid CNN-Mamba multi-scale attention. *Pattern Recognition*, 167:111723. https://doi.org/10.1016/j.patcog.2025.111723

Zhou SZ, Xia YX, Qi MZ, et al., 2025. Transformed workspace adaptive mapping based master-slave operation control for hydraulic manipulator. *IEEE Transactions on Industrial Electronics*, 72(8):8240-8250. https://doi.org/10.1109/TIE.2024.3525099